Original Research Paper

Exploration of the structural, spectroscopic and thermal properties of double sulfate monohydrate NaSm(SO$_4$)$_2$·H$_2$O and its thermal decomposition product NaSm(SO$_4$)$_2$

Yuriy G. Denisenko [a,b,c], Alexander E. Sedykh [b], Sofia A. Basova [c], Victor V. Atuchin [d,e,f,*],
Maxim S. Molokeev [g,h,i], Aleksandr S. Aleksandrovsky [j,k], Alexander S. Krylov [l], Aleksandr S. Oreshonkov [h,l],
Nikolay A. Khritokhin [c], Elena I. Sal'nikova [c,m], Oleg V. Andreev [c,n], Klaus Müller-Buschbaum [b,o]

[a] Department of General and Special Chemistry, Industrial University of Tyumen, Tyumen 625000, Russia
[b] Institute of Inorganic and Analytical Chemistry, Justus-Liebig-University Giessen, Heinrich-Buff-Ring 17, 35392 Giessen, Germany
[c] Department of Inorganic and Physical Chemistry, Tyumen State University, Tyumen 625003, Russia
[d] Laboratory of Optical Materials and Structures, Institute of Semiconductor Physics, SB RAS, Novosibirsk 630090, Russia
[e] Research and Development Department, Kemerovo State University, Kemerovo 650000, Russia
[f] Department of Applied Physics, Novosibirsk State University, Novosibirsk 630090, Russia
[g] Laboratory of Crystal Physics, Kirensky Institute of Physics, Federal Research Center KSC SB RAS, Krasnoyarsk 660036, Russia
[h] Siberian Federal University, Krasnoyarsk 660041, Russia
[i] Department of Physics, Far-Eastern State Transport University, Khabarovsk 680021, Russia
[j] Laboratory of Coherent Optics, Kirensky Institute of Physics Federal Research Center KSC SB RAS, Krasnoyarsk 660036, Russia
[k] Laboratory of Photonics and Laser Technology, Siberian Federal University, Krasnoyarsk 660041, Russia
[l] Laboratory of Molecular Spectroscopy, Kirensky Institute of Physics Federal Research Center KSC SB RAS, Krasnoyarsk 660036, Russia
[m] Research Department, Northern Trans-Ural State Agricultural University, Tyumen 625003, Russia
[n] Laboratory of the Chemistry of Rare Earth Compounds, Institute of Solid State Chemistry, UB RAS, Ekaterinburg 620137, Russia
[o] Center for Materials Research (LaMa), Justus-Liebig-University Giessen, Heinrich-Buff-Ring 16, 35392 Giessen, Germany

A B S T R A C T

Samarium-sodium double sulfate crystalline hydrate NaSm(SO$_4$)$_2$·H$_2$O was obtained by the crystallization from an aqueous solution containing equimolar amounts of ions. The anhydrous salt of NaSm(SO$_4$)$_2$ was formed by a thermally induced release of the equivalent of water from NaSm(SO$_4$)$_2$·H$_2$O. The kinetic parameters of thermal decomposition were determined (E_a = 102 kJ/mol, A = 9·10^6). The crystal structures of both compounds were refined from the X-ray powder diffraction data. Sulfate hydrate NaSm(SO$_4$)$_2$·H$_2$O crystallizes in the trigonal symmetry, space group $P3_121$ (a = 6.91820(3) and c = 12.8100(1) Å, V = 530.963(7) Å^3). The anhydrous salt crystallizes in the triclinic symmetry, space group P-1 (a = 6.8816(2), b = 6.2968(2) and c = 7.0607(2) Å, α = 96.035(1), β = 99.191(1) and γ = 90.986 (1)°, V = 300.17(1) Å^3). The vibrational properties of compounds are mainly determined by the sulfate group deformations. The luminescence spectra of both sulfates are similar and are governed by the transitions of samarium ions $^4G_{5/2} \rightarrow {}^6H_J$ (J = 5/2, 7/2, 9/2 and 11/2). The anhydrous sulfate is stable up to 1100 K and undergoes an almost isotropic expansion when heated. After 1100 K, the compound decomposes into Sm$_2$(SO$_4$)$_3$ and Na$_2$SO$_4$.

© 2021 The Society of Powder Technology Japan. Published by Elsevier B.V. and The Society of Powder Technology Japan. All rights reserved.

1. Introduction

Rare-earth elements (REE) and their compounds, possessing a number of useful properties, are widely used in industry and are present in many technical devices. The extended applications spectrum of the compounds of rare-earth elements are provided by such factors as their specific electronic structure and unique spectroscopic properties, diverse structural and thermal chemistry and anomalous physicochemical properties [1-12]. The first data on rare-earth sulfates belong to the beginning of the 19th century when Berzelius and Heesinger obtained individual preparations of various cerium sulfates [13]. Later, for sulfates of various

compositions, a number of valuable properties were discovered. Simple and complex sulfates are applied in the separation of rare-earth concentrates [14-19]. In several studies, the catalytic properties of REE sulfates were described with respect to redox processes in organic systems [20,21]. However, many physico-chemical parameters of rare-earth sulfates are hidden and have not ever been discussed anywhere. In particular, only fragmental information is available on the crystal-chemical properties of binary REE sulfates with monovalent cations [2,12,22-33].

Sm^{3+}-doped materials are of particular interest in photonics and laser technology due to their intense photoluminescence in the visible spectral region. In particular, the reddish-orange emission of Sm^{3+}ions is characterized by a high intensity, large cross-section of stimulated emission, high quantum efficiency and a very low probability of nonradiative decay, which are the desirable properties in creating luminescent and laser materials [34-42]. It could be pointed out, however, that the assessment of the effects of the nearest environment in the crystal lattice at a low concentration of doped ions is frequently sophisticated because, in many complex hosts, the substitution mechanisms are not trivial and it is difficult to relate properly the crystallographic and photoluminescence properties of activator ions. Generally, in the case of nonisovalent ion substitution, the generation of cation and/or anion defects accompanied by phase transitions is possible and it drastically complicates the understanding of the optical properties of doped crystals [43-52]. Thus, to see the basic relations between structural and physical characteristics, the increasing attention of researchers is focused on stoichiometric crystalline phases, where the crystallographic environment of cations can be precisely determined by the conventional methods of structural analysis [5,53-59]. In this strategy, the present work is aimed at the synthesis and exploration of structural and spectroscopic properties of NaSm(SO$_4$)$_2$·H$_2$O and its thermal decomposition product NaSm(SO$_4$)$_2$. First, NaSm(SO$_4$)$_2$·H$_2$O was prepared by the chemical reaction method. Then, anhydrous sulfate NaSm(SO$_4$)$_2$ was obtained by annealing in the air. The crystal structures of both compounds were determined by the X-ray diffraction analysis. The vibrational and photoluminescence properties of NaSm(SO$_4$)$_2$·H$_2$O and NaSm(SO$_4$)$_2$ were evaluated with the use of conventional experimental methods. The thermophysical characteristics of NaSm(SO$_4$)$_2$ were determined in the temperature range of 303–703 K.

2. Methods and materials

Dry salts NaNO$_3$ (ultrapure, Vekton Ltd., Russia), Sm(NO$_3$)$_3$·6H$_2$O (ultrapure 99.999%, Merck KGaA, Germany) and concentrated sulfuric acid (ultrapure 98%, Vekton Ltd., Russia) were used to prepare working solutions. The solutions were prepared with the use of double-distilled deionized water (χ = 0.1 mS/cm). The volumes of liquids were measured at the accuracy of 0.1 mL. Solid reagents were weighed on an analytical balance at the accuracy of 0.1 mg. Sulfate monohydrate NaSm(SO$_4$)$_2$·H$_2$O was synthesized by a slow evaporation of the water solution containing stoichiometric amounts of ions. For this, in a glass beaker, 10 mL of the NaNO$_3$ (C(Na$^+$) = 1 mol/L) solution, 10 mL of the Sm(NO$_3$)$_3$ (C(Sm^{3+}) = 1 mol/L) solution and 10 mL of the H$_2$SO$_4$ (C (SO$_4^{2-}$) = 2 mol/L) solution were mixed. The obtained solution was left in a desiccator over silica gel. In 12 h, the crystals precipitated from the mother liquor.They were filtered on a glass filter, washed with ice water, dried between filter paper sheets and kept in an empty desiccator to a constant weight. The obtained product was identified by the powder X-ray diffraction analysis. The NaSm(SO$_4$)$_2$·H$_2$O calcination in a muffle furnace at 800 K in the air for 10 h results in the formation of anhydrous sulfate NaSm(SO$_4$)$_2$. The dehydration reaction

product was identified by the powder X-ray diffraction and thermogravimetric analysis. The photos of the synthesized samples of NaSm(SO$_4$)$_2$·H$_2$O and NaSm(SO$_4$)$_2$ are presented in Fig. 1S. The light-orange tint observed for the samples is a characteristic color of Sm^{3+}-containing oxides [60]. When synthesizing, one should unquestionably observe the general rules of work in a chemical laboratory, as well as special rules for working with oxidants (nitrate solutions) and corrosive substances (sulfuric acid).

The high-resolution powder X-ray diffraction patterns for Rietveld analysis were collected at room temperature with a Bruker D8
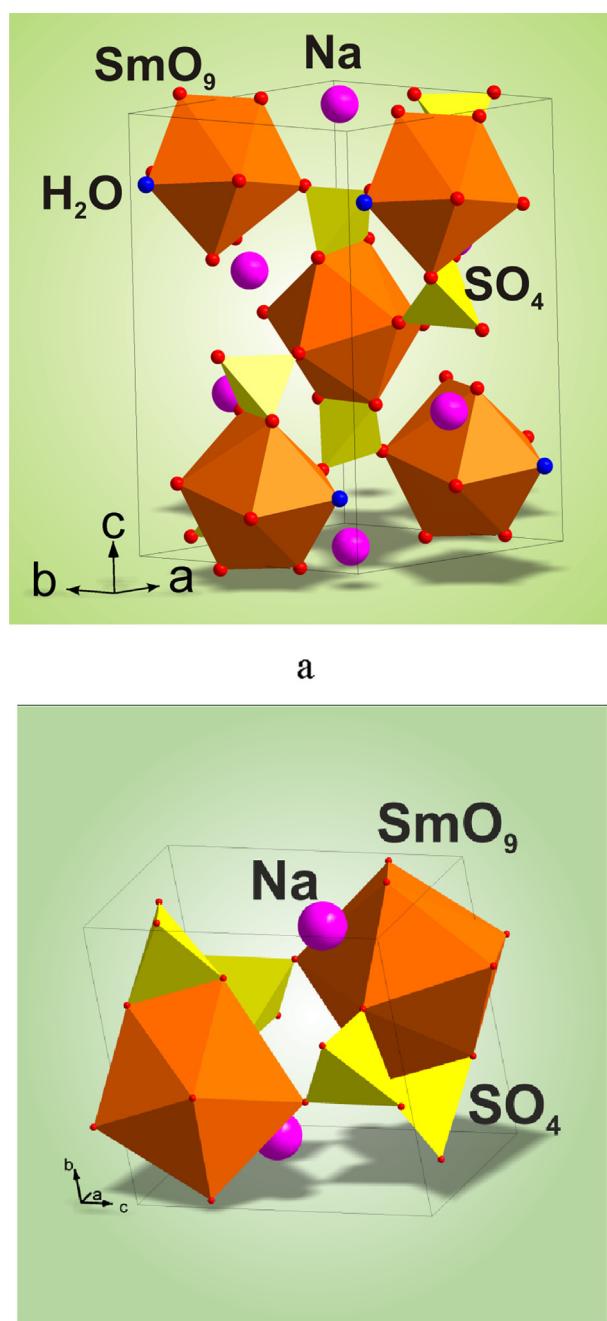

Fig. 1. Crystal structures of (a) NaSm(SO$_4$)$_2$·H$_2$O and (b) NaSm(SO$_4$)$_2$. Oxygen atoms are shown in red color, and, in structure (a), the oxygen atoms of H$_2$O are given in blue color. Unit cells are outlined. The lone atoms are omitted for clarity, except for Na atoms. (For interpretation of the references to color in this figure legend, the reader is referred to the web version of this article.)

ADVANCE powder diffractometer (Cu-Kα radiation) and linear VANTEC detector. The step size of 2θ was 0.02°, and the counting time was 5 s per step. The Rietveld refinement was performed using the TOPAS 4.2 program [61]. The $NaSm(SO_4)_2$ powder diffraction data were recorded in the temperature range of 303–703 K using an Anton Paar heating attachment. The 2θ range of 10-90° was measured with the 0.6 mm divergence slit, step size of 2θ = 0.016° and the counting time of 0.3 s per step. The samples morphology was studied using a JEOL JSM-6510LV scanning electron microscope. The powder samples were deposited on a conductive substrate (carbon tape) and covered with a nanometer gold layer (99.9%) to prevent the electrostatic charging of the sample.

The thermal analysis was carried out by means of DSC (differential scanning calorimetry) in the argon flow on a Simultaneous Thermal Analysis (STA) equipment 499 F5 Jupiter NETZSCH (Germany). The powder samples were inserted into alumina crucibles. The heating rate of 3 K/min was applied in the measurements. For the enthalpy determination, the equipment was initially calibrated with the use of standard metal substances, such as In, Sn, Bi, Zn, Al, Ag, Au and Ni. The heat effect peaks were determined with the package Proteus 6 2012. To investigate the decomposition kinetics, additional studies were performed at the heating rates of 5, 7 and 10 K/min. The kinetic parameters determination was based on the Kissinger formula in the linearized form [62]:

$$\frac{-1}{T} = \frac{1}{E}\hat{A} \cdot Rln\frac{b}{T^2} - \frac{R}{E}ln\frac{AR}{E}$$

where T is the temperature with a maximum reaction rate; b - heating rate, dps; E - activation energy; A - preexponential factor. The representative examples of the formula application to topochemical processes can be found elsewhere [63-65].

Fourier-transformed infrared spectroscopy (FTIR) was carried out with the use of a Fourier Transform Infrared Spectrometer FSM 1201. The sample for the investigation was prepared as a tablet with the addition of annealed KBr. The unpolarized Raman spectra were collected using an i-Raman Plus spectrometer at the laser excitation wavelength of 785 nm.

The photoluminescence excitation and emission spectra were recorded at room temperature and 77 K using a Horiba-Jobin-Yvon Fluorolog 3 spectrophotometer equipped with double-grated monochromators for excitation and emission, a xenon short-arc lamp, photomultiplier tube and a time-correlated single-photon counting (TCSPC) upgrade. The measurements at 77 K were performed in a special quartz glass Dewar assembly. The excitation and emission spectra were corrected for the spectral response of the monochromators and the detector using spectral corrections provided by the manufacturer. The excitation spectra were additionally corrected for the spectral distribution of the lamp intensity by the use of a photodiode reference detector. The emission spectra were measured using the excitation wavelength of 402 nm. The excitation spectra were recorded for the emission wavelength of 595 nm together with an edge filter (Newport, cut-off 455 nm).

3. Results and discussion

3.1. Crystal chemistry

As both compounds, $NaSm(SO_4)_2 \cdot H_2O$ and $NaSm(SO_4)_2$, were obtained as crystalline bulk powders, the structure refinement was made by the Rietveld refinement on the respective X-ray powder data. For both of them, potentially isotypic sodium lanthanide double salts are known in the literature [26,66]. All $NaSm(SO_4)_2$·$\cdot H_2O$ reflections were indexed by the trigonal cell ($P3_121$) with the parameters close to those of $NaCe(SO_4)_2 \cdot H_2O$ [66]. All reflec-

tions of $NaSm(SO_4)_2$ were indexed by the triclinic cell (P-1) with the parameters close to those of $NaNd(SO_4)_2$ [26]. Therefore, the structures of $NaCe(SO_4)_2 \cdot H_2O$ and $NaNd(SO_4)_2$ were taken as the starting models for Rietveld refinements. The sites of Ce^{3+} and Nd^{3+} ions were replaced by Sm^{3+} ions, respectively (Fig. 1). All thermal parameters of ions were refined isotropically. Moreover, all O^{2-} ions were refined with the same thermal paramater in order to minimize the epy number of refined parameters. The refinements were stable and gave low R-factors (Table 1, Fig. 2). The atom coordinates and the main bond lengths are given in Tables 2 and 3, respectively.

In the structure of $NaSm(SO_4)_2 \cdot H_2O$, the Sm^{3+} ions are coordinated by nine oxygen atoms, resulting in the formation of a coordination polyhedron shaped as a three-capped trigonal prism. The coordination involves seven sulfate groups and one water molecule. One sulfate group coordinates the samarium ion as a chelate. The Na^+ ions are eight-coordinated by the oxygen atoms of the six sulfate groups, two of which bind sodium ions as chelates. In the structure of $NaSm(SO_4)_2$, the Sm^{3+}ion is also nine-coordinated by oxygen atoms of sulfate groups, but the coordination number of Na atom decreases to seven, compared to that in $NaSm(SO_4)_2 \cdot H_2O$. The removal of crystal hydrate water molecules leads to an increase in the interconnection of the anhydrous salt structure and increased deformation of coordination polyhedra. The averaged bond length values correspond to the sums of ionic radii of the atoms forming the bond.

Further details of the crystal structures may be obtained from Fachinformationszentrum Karlsruhe, 76,344 Eggenstein-Leopoldshafen, Germany (fax: (+49)7247–808-666; E-mail: crystdata@fiz-karlsruhe.de; http://www.fiz-karlsruhe.de/request_for_deposited_data.html on quoting the deposition number CSD-2083429–2083430.

The family of isostructural compounds $NaLn(SO_4)_2 \cdot H_2O$ (Ln = REE) crystallized in trigonal space group $P3_121$ is relatively wide and covers the range from La to Dy [26,66-71]. In this range, the structure remains unknown only for $NaPm(SO_4)_2 \cdot H_2O$. As to other REE and related elements, the available information on the existence and properties of $NaLn(SO_4)_2 \cdot H_2O$ is very scarce. On the one hand, there is a report about the chemical synthesis of $NaLn(SO_4)_2 \cdot H_2O$ (Ln = Y, Pr, Ho, Er, Tm, Yb and Pu) and the related XRD patterns were indexed in space group $P3_121$[72], but, on the other hand, the crystal structures of the compounds were not determined. Thus, the boundaries of the family of trigonal sulfates $NaLn(SO_4)_2 \cdot H_2O$ are a subject for further investigations. For comparison, the unit cell parameters of compounds $NaLn(SO_4)_2 \cdot H_2O$ (Ln = La, Ce, Nd, Sm, Eu, Gd, Tb, Dy) are listed in Table 1S and shown in Fig. 3. As it is seen in Fig. 3a,b, the dependences of the $NaLn(SO_4)_2 \cdot H_2O$ unit cell parameters on the ionic radius IR of the

Table 1
Main parameters of processing and refinement of the samples.

Compound	$NaSm(SO_4)_2 \cdot H_2O$	$NaSm(SO_4)_2$
Sp.Gr.	$P3_121$	P-1
a, Å	6.91820(3)	6.8816(2)
b, Å	–	6.2968(2)
c, Å	12.8100(1)	7.0607(2)
α, °	–	96.035(1)
β, °	–	99.191(1)
γ, °	–	90.986(1)
V, Å³	530.963(7)	300.17(1)
Z	3	2
2θ-interval, °	5–140	5–140
R_{wp}, %	5.25	4.14
R_p, %	3.72	3.12
R_{exp}, %	2.26	2.26
χ^2	2.32	1.84
R_B, %	2.00	1.77
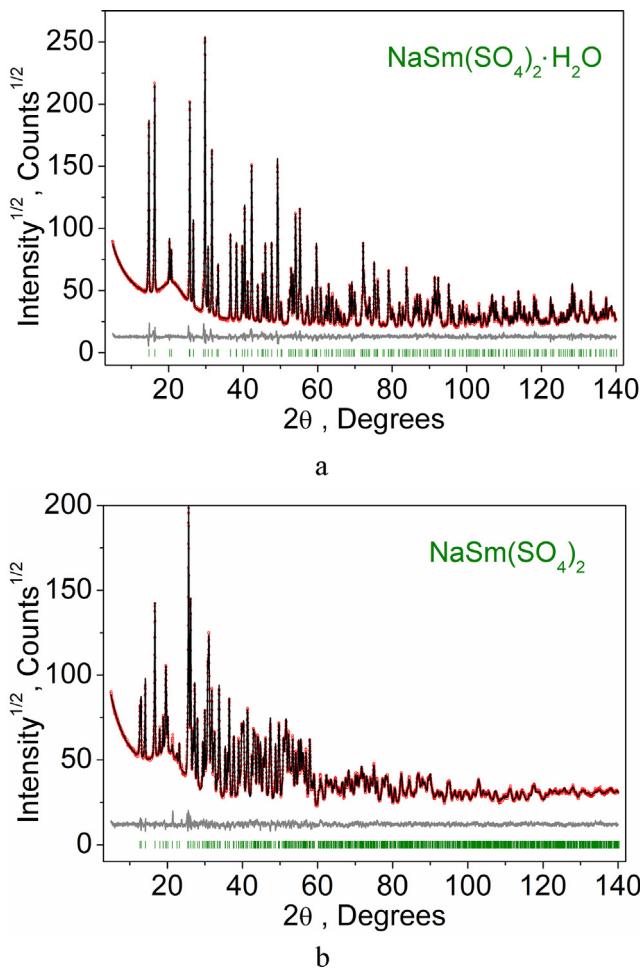
Fig. 2. Difference Rietveld plots of (a) NaSm(SO$_4$)$_2$·H$_2$O and (b) NaSm(SO$_4$)$_2$.

REE element are well described by linear functions $a = 5.1202 + 1.5882 \cdot IR$ and $c = 10.6174 + 1.9366 \cdot IR$. Accordingly, the related

variation of unit cell volume is also proportional to the IR value and can be given by linear function $V = 138.801 + 346.347 \cdot IR$ (Fig. 3c). Indeed, the volumes of H$_2$O and SO$_4$ units are practically persistent in all sulfates because of the short covalent bonds O-H and S-O. The Na-O bonds are highly ionic and their lengths are flexible, and, accordingly, the NaO$_8$ polyhedron size is controlled by external factors. Thus, it can be concluded that the unit cell volume variation in the NaLn(SO$_4$)$_2$·H$_2$O crystal series, due to the change of Ln^{3+} ion, is governed by the size of LnO$_9$ polyhedron, which volume can be considered as proportional to the efficient Ln^{3+} ion radius with coordination number 9 [73]. As it is shown in Fig. 3, the unit cell parameters of presently unknown compound NaPm(SO$_4$)$_2$·H$_2$O can be predicted by the linear interpolation using the known IR values [73], and the obtained values are given in Table 1S.

The situation with NaLn(SO$_4$)$_2$ compounds is even worse, and only the parameters of the triclinic structures of NaLa(SO$_4$)$_2$ and NaNd(SO$_4$)$_2$ can be found in the literature [25,26]. Thus, as for now, the set of known NaLn(SO$_4$)$_2$ compounds includes three crystals (Ln = La, Nd, Sm) and their structural parameters are given in Table 2S. However, it could be mentioned that, according to available structural information, the NaLa(SO$_4$)$_2$ structure type is different from that of NaLn(SO$_4$)$_2$ (Ln = Nd, Sm) and the change of the structure type can be reasonably supposed on the substitution of Nd by Pr, Ce and La in NaLn(SO$_4$)$_2$. The exact position of the boundary between these two crystal families is presently unclear and its determination is a subject of future experiments.

3.2. Vibrational and photoluminescence spectra

The Raman and Infrared spectra of NaSm(SO$_4$)$_2$ and NaSm(SO$_4$)$_2$·H$_2$O powders are shown in Fig. 4. The mechanical representation [74] at the Γ = 0 point of the Brillouin zone (BZ) for triclinic NaSm(SO$_4$)$_2$ is $\Gamma_{vibr} = 36A_g + 36A_u$, where Raman active modes are g labeled and the Infrared active modes are u labeled. The acoustic modes are $\Gamma_{vibr} = 3A_u$, and the remaining modes are optical ones. As to NaSm(SO$_4$)$_2$·H$_2$O, it can be seen in Table 2 that the fractional atomic coordinates of the hydrogen atom in NaSm(SO$_4$)$_2$·H$_2$O are not determined from the powder diffraction data. Taking into account the Wyckoff position of the H atom determined for isostructural single crystals [70] as 6c, the mechanical representation at the BZ center for trigonal NaSm(SO$_4$)$_2$·H$_2$O can be written as

Table 2
Fractional atomic coordinates and isotropic displacement parameters (Å^2) of the compounds.

	x	y	z	B_{iso}
NaSm(SO$_4$)$_2$·H$_2$O				
Na	0.4626(6)	0	1/3	0.76(8)
Sm	0	0.43455(12)	1/6	0.92(3)
S	0.5579(5)	0.5459(5)	0.25751(13)	0.86(4)
O1	0.7613(9)	0.5931(8)	0.1978(5)	1.14(7)
O2	0.375(1)	0.5065(8)	0.1865(6)	1.14(7)
O3	0.4889(8)	0.3618(8)	0.3321(6)	1.14(7)
O4	0.6170(8)	0.7414(8)	0.3225(5)	1.14(7)
O5	0	0.0761(12)	1/6	1.14(7)
NaSm(SO$_4$)$_2$				
Na	0.2998(7)	0.9462(9)	0.7169(7)	1.34(12)
Sm	0.19448(12)	0.36128(16)	0.20317(11)	0.94(5)
S1	0.2903(5)	0.4405(6)	0.7148(5)	1.27(6)
S2	0.1826(5)	0.8663(7)	0.2118(5)	1.27(6)
O1	0.0222(11)	0.0198(13)	0.2477(9)	0.58(8)
O2	0.1050(9)	0.6909(13)	0.0621(9)	0.58(8)
O3	0.2838(10)	0.3057(13)	0.8697(10)	0.58(8)
O4	0.1146(10)	0.5681(10)	0.6996(8)	0.58(8)
O5	0.3478(10)	0.9959(11)	0.1567(8)	0.58(8)
O6	0.2469(10)	0.7588(11)	0.3601(10)	0.58(8)
O7	0.2866(10)	0.3070(11)	0.5432(9)	0.58(8)
O8	0.4509(11)	0.6025(12)	0.7464(9)	0.58(8)

Table 3
Main interatomic distances (Å) of the compounds.

NaSm(SO₄)₂·H₂O			
Na—O1^i	2.893(7)	Sm—O4^{iv}	2.519(6)
Na—O2^i	2.604(7)	Sm—O5	2.480(7)
Na—O3	2.417(5)	S—O1	1.487(5)
Na—O4^{ii}	2.504(5)	S—O2	1.471(6)
Sm—O1^{iii}	2.429(5)	S—O3	1.468(6)
Sm—O2	2.396(5)	S—O4	1.462(6)
Sm—O3^{iv}	2.479(7)		
NaSm(SO₄)₂			
Na—O1^i	2.280(7)	Sm—O5^{vii}	2.559(6)
Na—O3^{ii}	2.415(9)	Sm—O6	2.623(6)
Na—O4	2.663(8)	Sm—O7	2.444(6)
Na—O5^{iii}	3.052(7)	Sm—O8^{viii}	2.413(7)
Na—O5^{iv}	2.454(7)	S1—O3	1.459(8)
Na—O6	2.634(8)	S1—O4	1.459(7)
Na—O7^{ii}	2.689(8)	S1—O7	1.396(7)
Na—O8	2.431(8)	S1—O8	1.465(7)
Sm—O1	2.510(7)	S2—O1^{ii}	1.514(8)
Sm—O2	2.442(7)	S2—O2	1.475(8)
Sm—O2^v	2.545(6)	S2—O5	1.512(7)
Sm—O3^{vi}	2.518(7)	S2—O6	1.327(7)
Sm—O4^i	2.372(6)		

Symmetry codes for NaSm(SO₄)₂·H₂O: (i) -x + 1, -x + y, -z + 1/3; (ii) × ,y-1, z; (iii) x-1, y, z; (iv) -x + y, -x + 1, z-1/3.
Symmetry codes for NaSm(SO₄)₂: (i) -x, -y + 1, -z + 1; (ii) × ,y + 1, z; (iii) × ,y, z + 1; (iv) -x + 1, -y + 2, -z + 1; (v) -x, -y + 1, -z; (vi) × ,y, z-1; (vii) × ,y-1, z; (viii) -x + 1, -y + 1, -z + 1.

Γ_{vibr} = 21A_1 + 24A_2 + 44E. The acoustic modes are Γ_{vibr} = A_2 + E, and the remaining modes are optical. The Raman and Infrared modes are Γ_{Raman} = 21A_1 + 44E and $\Gamma_{Infrared}$ = 23A_2 + 44E, respectively.

In Table S3, the correlation scheme is given for the SO₄ group with the T_d symmetry placed into the C_1 symmetry position of the NaSm(SO₄)₂ unit cell having the C_i symmetry [75]. According to Table S3, the numbers of Infrared and Raman active modes, related to the internal vibrations of SO₄ tetrahedra, are equal. It is clearly seen in Figure 2S(a) that the strong Raman bands at 995 and 1027 cm⁻¹, related to the symmetric vibrations of SO₄²⁻, correspond to weak bands in the Infrared spectrum and *vice versa*. Taking into account that NaSm(SO₄)₂ has two crystallographically independent SO₄²⁻ ions, we can conclude that two strong bands at 995 and 1027 cm⁻¹ (Fig. 4(a)) are related to the symmetric stretching of SO₄ tetrahedra. The number of antisymmetric stretching modes in the range of 1050–1200 cm⁻¹ should be equal to six and all of them appeared in the experimental spectrum. The antisymmetric and symmetric bending modes of SO₄²⁻ ions are in the ranges of 580–680 and 400–545 cm⁻¹, respectively. The rotational modes of SO₄ tetrahedra are located in the range of 200–235 cm⁻¹. The spectral bands below 190 cm⁻¹ are the translational modes of SO₄, Na, Sm and mixed vibrations of these structural units. It should be noted that the Raman spectrum of NaSm(SO₄)₂ is similar to the Raman spectrum of AgEu(SO₄)₂ [33] (Figure S3) excluding a triplet of luminescent $^5D_1$–$^7F_0$ lines of the Eu³⁺ ion luminescence. Both compounds are of triclinic symmetry (space group P-1) and have two crystallographically independent SO₄²⁻ groups in the unit cell.

The correlation between the vibrational modes of the SO₄ group with the T_d symmetry placed into the C_1 symmetry position of the NaSm(SO₄)₂·H₂O unit cell having the D_3 symmetry is shown in Table S4. The strongest Raman band at 1013 cm⁻¹ corresponds to the symmetric stretching of SO₄ tetrahedra. The IR peak at 1007 cm⁻¹ is related to the ν_1 vibration of the SO₄²⁻ unit too, but this vibration is antisymmetric through the cell. The bands in the range of 1045–1250 cm⁻¹ of the vibrational spectrum are the antisymmetric stretching vibrations of SO₄²⁻ ions. The antisymmetric bending vibrations of sulfate ions are observed between 550
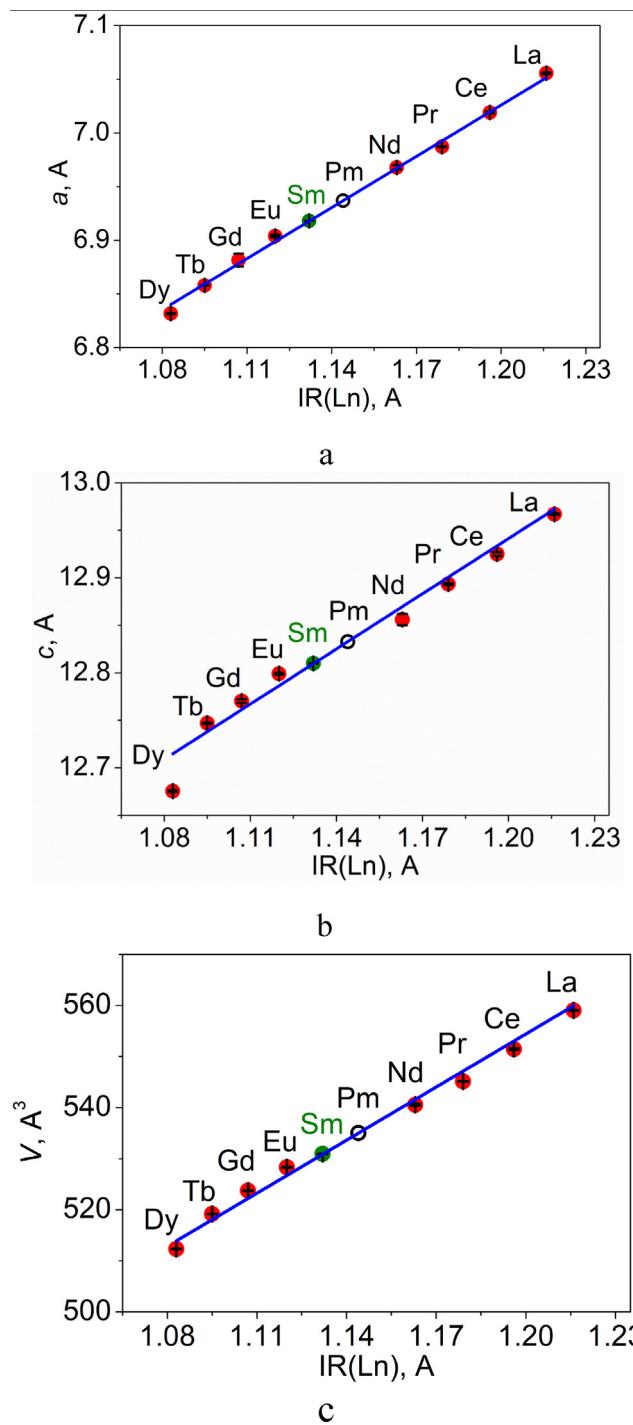

Fig. 3. Unit cell parameters (a) a, (b) c and (c) V as a function of ionic radius IR(Ln) in NaLn(SO₄)₂·H₂O compounds. Here, the experimental points are given in red and green colors, and the prediction is designated by an empty circle. (For interpretation of the references to color in this figure legend, the reader is referred to the web version of this article.)

and 700 cm⁻¹, while the symmetric bending vibrations are located between 400 and 520 cm⁻¹. The spectral band at 209 cm⁻¹ in the Raman spectrum is associated with the SO₄ rotations and the spectral band below 200 cm⁻¹ is attributed to the lattice vibrations. The number of observed bands in the vibrational spectra of NaSm(SO₄)₂·H₂O is less than that predicted by the factor group analysis; however, the lines related to the H₂O vibrations are clearly seen above the 1200 cm⁻¹ in the Infrared spectrum shown in

a

b
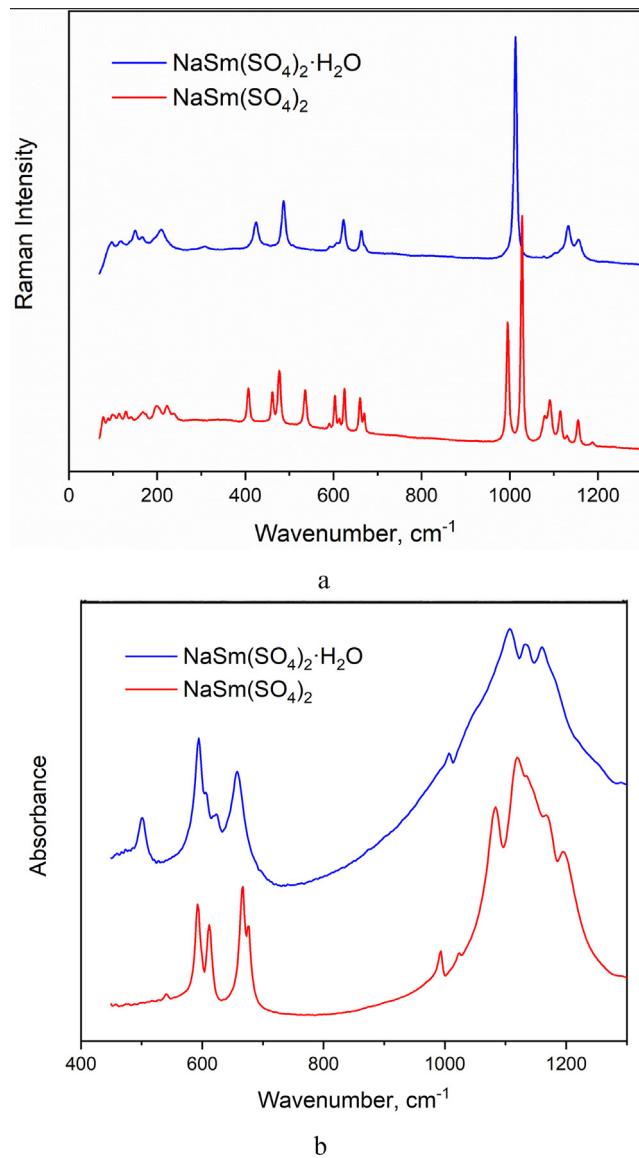
Fig. 4. (a) Raman and (b) IR spectra of $NaSm(SO_4)_2 \cdot H_2O$ and $NaSm(SO_4)_2$.

Figure S2(b). In the case of spectral band overlapping, the polarized Raman spectroscopy can provide information about vibrational modes with specified irreducible representations, but a single crystal sample is needed for the measurements.

The excitation and emission spectra of $NaSm(SO_4)_2 \cdot H_2O$ and $NaSm(SO_4)_2$ in the visible and UV spectral ranges are dominated by intra 4f-transitions, and it is typical of wide-bandgap dielectrics containing 4f ions. The emission spectra of both crystalline materials under study excited at 402 nm are presented in Fig. 5a,b. The excitation wavelength was set to 402 nm being in a resonance to the spin-allowed transition from the ground state $^6H_{5/2}$ to the $^6P_{3/2}$ state of the Sm^{3+} ion. The excited electrons from the $^6P_{3/2}$ level nonradiatively decay to the $^4G_{5/2}$ state. The luminescence spectra of both materials contain the transitions from the $^4G_{5/2}$ state to ^6H_J (J = 5/2, 7/2, 9/2, and 11/2) states, and the transition to $^6H_{7/2}$ is the most intense of them [76,77]. The CIE coordinates of the luminescence from both compounds are close to each other: (0.6, 0.4) for sodium samarium sulfate hydrate and (0.605, 0.395) for sodium samarium sulfate (Fig. 4S). The comparison of the spectra of each compound recorded at room temperature and at 77 K allows deducing that the internal structure of

individual bands is preserved in general features, and, therefore, it can be ascribed to the crystal field splitting of the degenerate sublevels of both starting and terminating energy states. A more pronounced splitting in $NaSm(SO_4)_2$, as compared to that in $NaSm(SO_4)_2 \cdot H_2O$, is noticeable even at room temperature and becomes evident at 77 K.

To give an insight into the difference of this band structure, the symmetry data for the crystalline structures under study can be taken into consideration. $NaSm(SO_4)_2 \cdot H_2O$ belongs to the trigonal crystal system, while $NaSm(SO_4)_2$ crystallizes in the triclinic space group. Sm^{3+} ions occupy a single site and they are coordinated by nine oxygen ions in both lattices. The local environment of the Sm^{3+} ion is of rather low symmetry: C_2 in $NaSm(SO_4)_2 \cdot H_2O$ and C_1 in $NaSm(SO_4)_2$. The examination of the crystallographic environment of Sm^{3+} ions shows that, despite a certain difference in symmetry, the decrease of crystal field-induced oscillator strength in $NaSm(SO_4)_2$ cannot be expected in reference to that in $NaSm(SO_4)_2 \cdot H_2O$. The difference of internal structure of individual bands in $NaLn(SO_4)_2 \cdot H_2O$ and $NaSm(SO_4)_2$ must be ascribed to the lowering of the local symmetry of Sm^{3+} ion from C_2 to C_1.

The photoluminescence excitation spectra recorded by monitoring the emission of $^4G_{5/2}-$ $^6H_{7/2}$ at 595 nm for Sm^{3+} ions in $NaSm(SO_4)_2 \cdot H_2O$ are presented in Fig. 5c. They contain most of the bands common for the Sm^{3+} excitation in a number of hosts, the assignments of identified bands being presented. Surprisingly, these spectra show strong intensities for the spin-forbidden $^6H_{5/2} - ^4D_{3/2}$ band peaking at 362 nm, while the neighboring spin-allowed $^6H_{5/2} - ^6P_{3/2}$, $^6H_{5/2} - ^6P_{7/2}$ and spin-forbidden $^6H_{5/2} - ^4D_{7/2}$ bands demonstrate almost the same order of magnitude. The spin-forbidden $^6H_{5/2} - ^4F_{3/2}$ and $^6H_{5/2} - ^4G_{5/2}$ bands exhibit their extremely small excitation efficiency, while another set of spin-forbidden transitions, namely, $^6H_{5/2} - ^4I_{9/2}$, $^6H_{5/2} - ^4I_{9/2}$ and $^6H_{5/2} - ^4M_{17/2}$, is about 2–6 times less efficient than that of the spin-allowed $^6H_{5/2} - ^6P_{3/2}$ band at 402 nm. Therefore, most of the bands in the excitation spectrum of Sm^{3+} ion in the crystalline lattice form the band sequence covering the range of efficient generation of GaN LEDs protruding from the near UV range to the blue one. Partial equalization of the intensities of some spin-forbidden transitions with the intensities of spin-allowed transitions in the excitation spectra of both compounds must be ascribed to low local symmetry at Sm sites in their crystalline structure. The crystal field low-symmetry components produce not only the mixing of the states with different J values, but the mixing of states with different spin or even admixing of high-lying charge transfer states. The excitation spectrum of the Sm^{3+} ion in $NaSm(SO_4)_2$ is, in general features, quite similar to that of $NaSm(SO_4)_2 \cdot H_2O$. Therefore, we must note that the reduction of the local symmetry of samarium ion in $NaSm(SO_4)_2$ exhibits a smaller effect than that in the emission spectra. However, as one can see in Fig. 5d, the short-wavelength part of the $NaSm(SO_4)_2$ excitation spectrum contains the additional intense wide band below 300 nm that is absent in $NaSm(SO_4)_2 \cdot H_2O$. This band cannot be ascribed to the f-f transitions of Sm^{3+} ion and may be suggested to be a kind of allowed transitions like the charge transfer or f-d ones. However, for Sm^{3+}-ions, these transitions are expected to lie at sufficiently lower wavelengths. Therefore, the origin of strong excitation of $NaSm(SO_4)_2$ below 300 nm needs an additional study.

3.3. Thermochemical properties

The results of DSC/TG measurements carried out for $NaSm(SO_4)_2 \cdot H_2O$ are shown in Fig. 6. A set of thermal effects combining the thermal properties of $NaSm(SO_4)_2 \cdot H_2O$ and $NaSm(SO_4)_2$ was obtained. The interpretation of the observed effects is given in Table 4. According to the DSC and TG data, in the temperature range of 500–650 K, $NaSm(SO_4)_2 \cdot H_2O$ is dehydrated in one stage
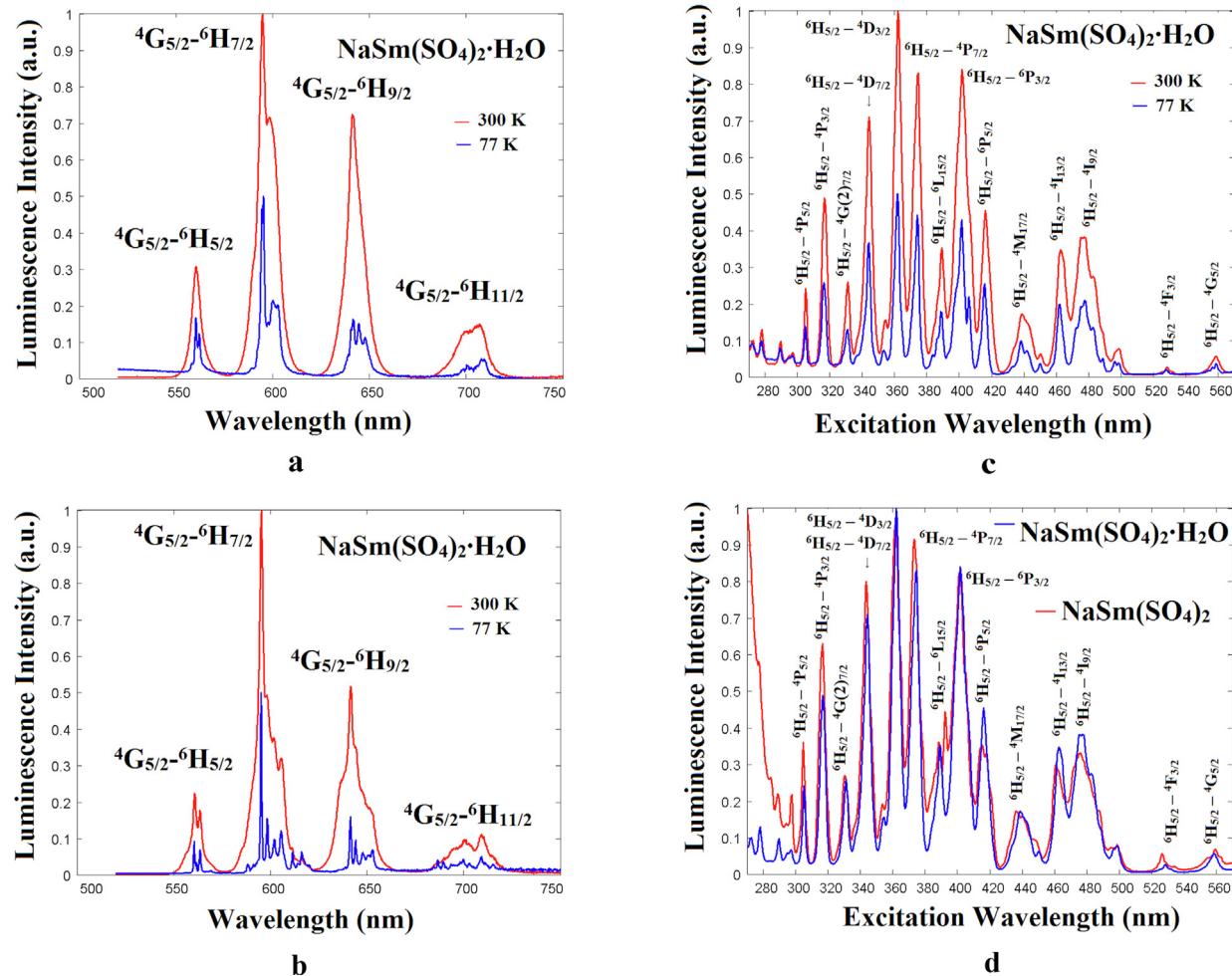
**Fig. 5.** Emission spectra of (a) NaSm(SO$_4$)$_2$·H$_2$O and (b) NaSm(SO$_4$)$_2$. (c) Excitation spectra of NaSm(SO$_4$)$_2$·H$_2$O. (d) Comparison of NaSm(SO$_4$)$_2$·H$_2$O and NaSm(SO$_4$)$_2$ excitation spectra.
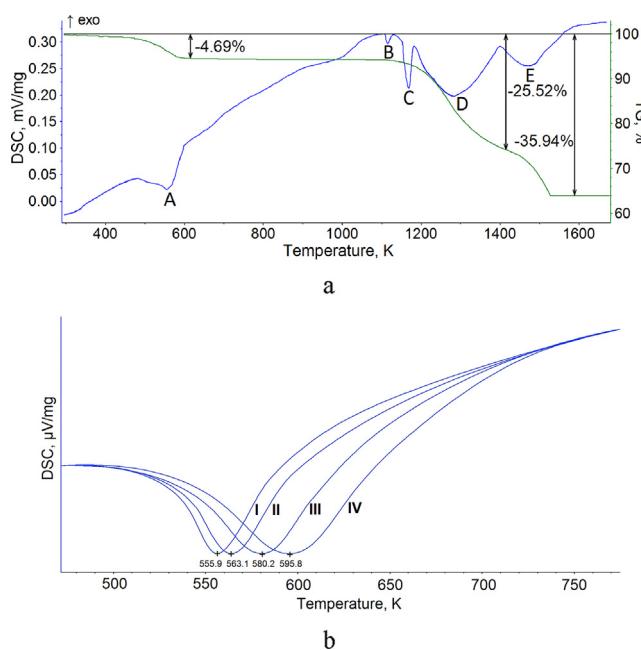
Fig. 6. (a) DSC/TG curves recorded for NaSm(SO$_4$)$_2$·H$_2$O and (b) thermal effects of dehydration at different theating rates (heating rates: I − 3 K/min, II − 5 K/min, III − 10 K/min, IV − 15 K/min).

(effect A). The polycrystalline dehydration product is anhydrous NaSm(SO$_4$)$_2$, which is stable up to 1110 K, and, above this temperature, NaSm(SO$_4$)$_2$ decomposes into simple sulfates Na$_2$SO$_4$ and Sm$_2$(SO$_4$)$_3$ (effect B). Then, the simple sulfates behave as individual components. Sodium sulfate melts in the temperature range of 1150–1175 K [78] (effect C) and remain in this state until the end of the analysis. Samarium sulfate Sm$_2$(SO$_4$)$_3$ decomposes immediately after its formation, and this process determines the mass loss of the sample in the temperature range of 1110–1540 K. The thermal decomposition of samarium sulfate proceeds in two stages at ∼ 1300 and ∼ 1460 K, related to the subsequent formation of Sm$_2$O$_2$SO$_4$ oxysulfate (effect D) and Sm$_2$O$_3$ oxide (effect E), respectively [79].

The established sequence of thermal processes in NaSm(SO$_4$)$_2$·H$_2$O is similar to that observed earlier in NaBi(SO$_4$)$_2$·H$_2$O. However, the lack of DSC data in [80] does not allow us to compare the processes proceeding at the dehydration stage of NaBi(SO$_4$)$_2$·H$_2$O. At the same time, the NaSm(SO$_4$)$_2$·H$_2$O thermal decomposition mechanism is significantly different from that obtained for the isostructural compound AgEu(SO$_4$)$_2$·H$_2$O [81] in view of different binding effects in the structure and the difference of the electronic structures of Na$^+$ and Ag$^+$ ions. The kinetic characteristics of the NaSm(SO$_4$)·H$_2$O dehydration process (Fig. 6b) were calculated using the Kissinger equation as equal to E_A = 102 kJ/mol, $A = 9 \cdot 10^6$, and the values can be compared to the characteristics of other related compounds. The parameters of the dehydration

Table 4
Thermal effects in $NaSm(SO_4)_2 \cdot H_2O$.

Thermal effect	Reaction	Reference	Loss of mass, %	
			Theor.	Exp.
A	$NaSm(SO_4)_2 \cdot H_2O \rightarrow NaSm(SO_4)_2 + H_2O$	This work	4.68	4.69
B	$2NaSm(SO_4)_3 \rightarrow Na_2SO_4 + Sm_2(SO_4)_3$	This work	0.0	0.0
C	$Na_2SO_{4\ (sol)} \rightarrow Na_2SO_{4\ (liq)}$	[78]	0.0	0.0
D	$Sm_2(SO_4)_3 \rightarrow Sm_2O_2SO_4 + 2SO_2 + O_2$	[79]	25.55	25.52
E	$Sm_2O_2SO_4 \rightarrow Sm_2O_3 + SO_2 + {}^1/_2 O_2$	[79]	35.98	35.94
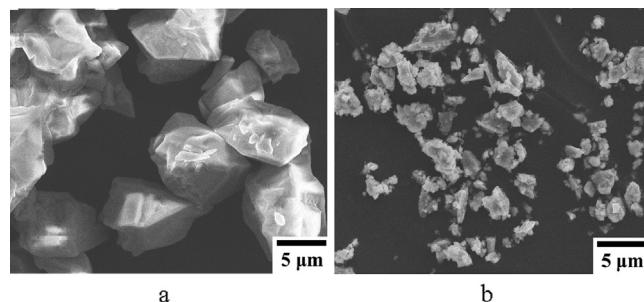
Fig. 7. SEM images of (a) $NaSm(SO_4)_2 \cdot H_2O$ and (b) $NaSm(SO_4)_2$.

process of $Eu_2(SO_4)_3 \cdot 8H_2O$, space group $C2/c$, were determined previously [56]. Thus, $NaSm(SO_4)_2 \cdot H_2O$ shows a significantly higher activation energy $E_A = 102$ kJ/mol, as compared to $E_A = 71$ kJ/mol in $Eu_2(SO_4)_3 \cdot 8H_2O$. The dehydration peak, reflecting the kinetic stability, is much more diffused in $NaSm(SO_4)_2 \cdot H_2O$ (Fig. 6) than that in $Eu_2(SO_4)_3 \cdot 8H_2O$, and it indicates a higher kinetic stability of $NaSm(SO_4)_2 \cdot H_2O$. The higher activation energy of the $NaSm(SO_4)_2 \cdot H_2O$ dehydration, as compared to that of $Eu_2(SO_4)_3 \cdot 8H_2O$, is compensated by a higher (almost an order of magnitude)

pre-exponential factor A value (the compensation effect common in such cases): $9 \cdot 10^6$ for $NaSm(SO_4)_2 \cdot H_2O$ and $1 \cdot 10^6$ for $Eu_2(SO_4)_3 \cdot 8H_2O$. This reveals a higher entropy of activation of $NaSm(SO_4)_2 \cdot H_2O$ dehydration, which is consistent with a higher symmetry of its structure i.e. the hexagonal crystal system for $NaSm(SO_4)_2 \cdot H_2O$ and monoclinic for $Eu_2(SO_4)_3 \cdot 8H_2O$.

According to the SEM measurements, the faceted $NaSm(SO_4)_2 \cdot H_2O$ particles are 3–7 μm in size (Fig. 7a) and they disintegrate into smaller fragments as a result of dehydration. The particle size of anhydrous $NaSm(SO_4)_2$ does not exceed 4 μm (Fig. 7b). As it can be assumed, the $NaSm(SO_4)_2 \cdot H_2O$ particles disintegration is caused by the diffusion nature of the topochemical dehydration process.

The thermophysical properties of $NaSm(SO_4)_2$ were determined for the temperature range of 303–703 K, and the dependences of the unit cell parameters on temperature are shown in Fig. 8. As it can be seen, heating the $NaSm(SO_4)_2$ sample from 143 to 703 K leads to a continuous increase of all three cell parameters (Table S1). Above this, there is no indication of a phase transition in triclinic $NaSm(SO_4)_2$ in the temperature range of 303–703 K and it is in a good relation with the results of the DSC measurements. The linear thermal expansion coefficients of cell parameters a, b and c are similar in magnitude and, therefore, the compound expands almost isotropically, as shown in Fig. 9. It should be mentioned that, due to the low structure symmetry, the direction of the strongest thermal
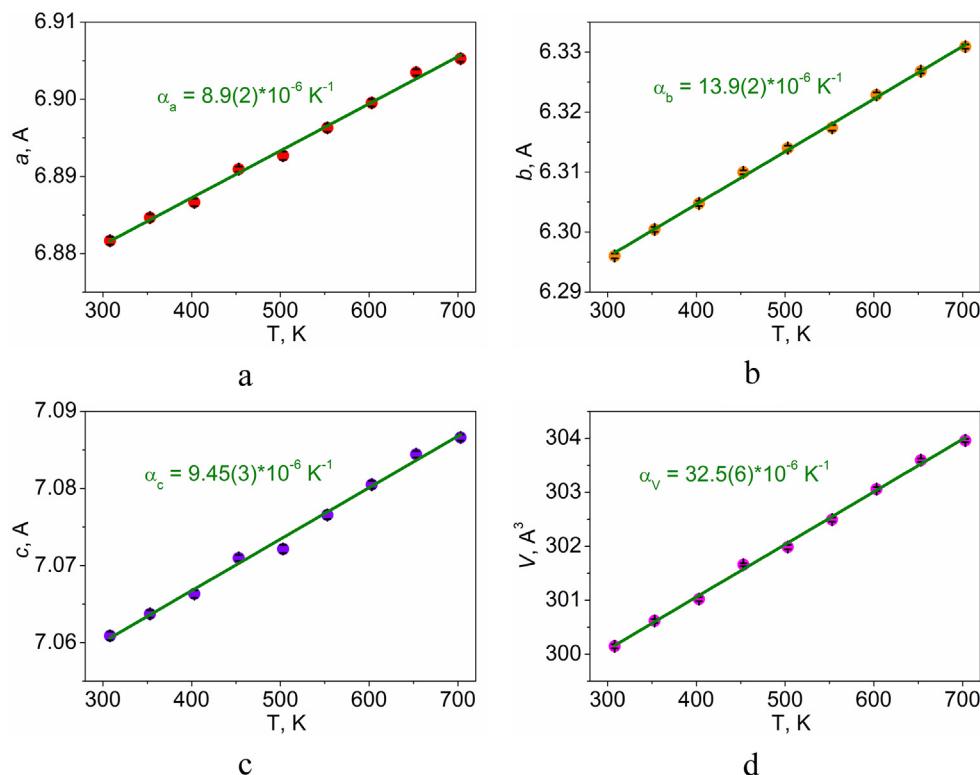

Fig. 8. Temperature dependences of the $NaSm(SO_4)_2$ cell parameters (a) $a(T)$; (b) $b(T)$; (c) $c(T)$; (d) $V(T)$.
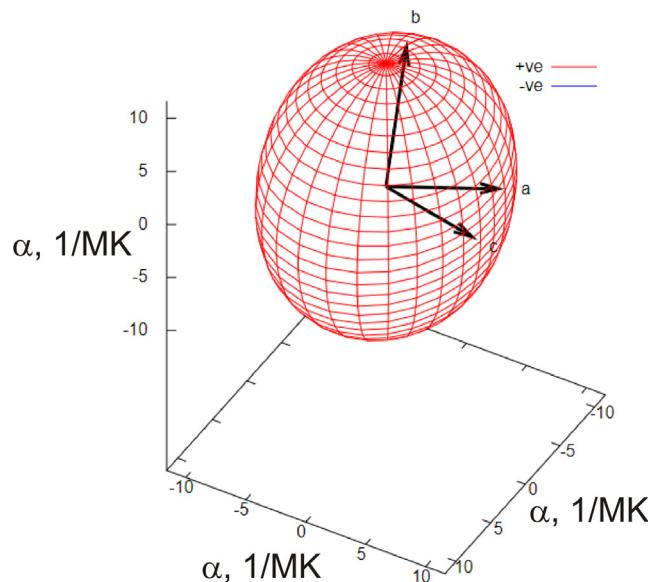
Fig. 9. Thermal expansion tensor of $NaSm(SO_4)_2$.

expansion in $NaSm(SO_4)_2$ does not coinside with any crystallographic axis, and it is close to the crystallographic axis b.

4. Conclusions

In the present study, the structural, spectroscopic and thermal characteristics of two complex sulfates $NaSm(SO_4)_2 \cdot H_2O$ and $NaSm(SO_4)_2$ were evaluated for the first time. The method of reducing the amount of the solvent used to obtain $NaSm(SO_4)_2 \cdot H_2O$ as a crystalline hydrate makes it possible to obtain a polycrystalline product of good structural quality. As obtained by the Rietveld refinement of X-ray powder data, the compound crystallizes in in the space group $P3_121$, similar to other known $NaLn(SO_4)_2 \cdot H_2O$ compounds. When $NaSm(SO_4)_2 \cdot H_2O$ is heated, the compound loses the water equivalent in the temperature range of 500–1100 K with the formation of anhydrous salt $NaSm(SO_4)_2$. The kinetic parameters of the dehydration reaction are determined by the symmetry of the crystalline hydrate structure. $NaSm(SO_4)_2$ crystallizes in triclinic space group P-1. Accordingly, the family of the known triclinic sulfates $NaLn(SO_4)_2$ is developed up to three members with Ln = La, Nd, Sm. The comparative analysis of available information opens a possibility to predict the existence and structural parameters of yet unknown crystals from the $NaLn(SO_4)_2 \cdot H_2O$ and $NaLn(SO_4)_2$ family, and that is a good basis for the activities in this research field.

The luminescence properties of $NaSm(SO_4)_2 \cdot H_2O$ and $NaSn(SO_4)_2$ were determined and they are dominated by the intra 4f-transitions of the Sm^{3+} ions. The excitation spectrum of the Sm^{3+} ion in $NaSm(SO_4)_2$ is, in general features, quite similar to that of $NaSm(SO_4)_2 \cdot H_2O$ and most of the bands in the Sm^{3+} ion excitation spectrum cover the range of efficient generation of GaN LEDs. However, the short-wavelength part of the $NaSm(SO_4)_2$ excitation spectrum contains an additional intense wide band below 300 nm that is absent in $NaSm(SO_4)_2 \cdot H_2O$. This band cannot be ascribed to the f-f transitions of the Sm^{3+} ion and may be suggested as being a kind of allowed transitions like the charge transfer or f-d ones. Therefore, the origin of strong $NaSm(SO_4)_2$ excitation below 300 nm needs an additional study, including the comparison of excitation spectra of different Sm^{3+}-containing crystals.

The nearly isotropic thermal expansion is observed in $NaSm(SO_4)_2$ and it is in a strong contrast to the one-dimension negative thermal expansion recently obtained in monoclinic $AgHo(SO_4)_2$.

This example emphasizes the general relation of that binary REE-containing sulfates are characterized by a diverse crystal chemistry, and their structure-related properties are strongly dependent on the combination of big cations. Thus, binary REE-containing sulfates are a promising chemical class for searching new crystals with specific thermophysical parameters.

Declaration of Competing Interest

The authors declare that they have no known competing financial interests or personal relationships that could have appeared to influence the work reported in this paper.

Acknowledgments

Appendix A. Supplementary material

Supplementary data to this article can be found online at https://doi.org/10.1016/j.apt.2021.08.009.

References

[1] B.K. Ponomarev, Magneto-electrical properties of rare earth molybdates, Ferroelectrics 280 (1) (2002) 95–117.
[2] M.S. Wickleder, Inorganic lanthanide compounds with complex anions, Chem. Rev. 102 (6) (2002) 2011–2088.
[3] S.V. Eliseeva, J.C.G. Bünzli, Rare earths: jewels for functional materials of the future, New J. Chem. 35 (2011) 1165–1176.
[4] Z. Xia, Y. Zhang, M.S. Molokeev, V.V. Atuchin, Structural and luminescence properties of yellow-emitting $NaScSi_2O_6$:Eu^{2+} phosphors: Eu^{2+} site preference analysis and generation of red emission by cooping Mn^{2+} for white-light-emitting diode applications, J. Phys. Chem. C 117 (2013) 20847–20854.
[5] V.V. Atuchin, A.S. Aleksandrovsky, O.D. Chimitova, T.A. Gavrilova, A.S. Krylov, M.S. Molokeev, A.S. Oreshonkov, B.G. Bazarov, J.G. Bazarova, Synthesis and spectroscopic properties of monoclinic α-$Eu_2(MoO_4)_3$, J. Phys. Chem. C 118 (28) (2014) 15404–15411.
[6] K. Müller-Buschbaum, Luminescent MOFs and frameworks, in Ref, Modul. Chem. Mol. Sci. Chem. Eng., Elsevier (2015), https://doi.org/10.1016/B978-0-12-409547-2.11493-3.
[7] D. Guyonnet, M. Planchon, A. Rollat, V. Escalon, J. Tuduri, N. Charles, S. Vaxelaire, D. Dubois, H. Fargier, Material flow analysis applied to rare earth elements in Europe, J. Clean. Prod. 107 (2015) 215–228.
[8] Chang Sung Lim, Aleksandr Aleksandrovsky, Maxim Molokeev, Alexandr Oreshonkov, Victor Atuchin, The modulated structure and frequency upconversion properties of $CaLa2(MoO4)4$:$Ho3+$/$Yb3+$ phosphors prepared by microwave cynthesis, Phys. Chem. Chem. Phys. 17 (2015) 19278–19287.
[9] Z. Xia, Q. Liu, Progress in discovery and structural design of color conversion phosphors for LEDs, Prog. Mater. Sci. 84 (2016) 59–117.
[10] S.H. Zottnick, J.R. Sorg, K. Müller-Buschbaum, C. Fouassier, Luminescence, in Encycl, Inorg. Bioinorg. Chem., Wiley (2019) 1–22, https://doi.org/10.1002/9781119951438.eibc0114.pub2.
[11] K. Takagi, Y. Hirayama, S. Okada, W. Yamaguchi, K. Ozaki, Novel powder processing technologies for production of rare-earth permanent magnets, Sci. Technol. Adv. Mater. 22 (1) (2021) 150–159.
[12] Y.G. Denisenko, V.V. Atuchin, M.S. Molokeev, N. Wang, X. Jiang, A.S. Aleksandrovsky, A.S. Krylov, A.S. Oreshonkov, A.E. Sedykh, S.S. Volkova, Z. Lin, O.V. Andreev, K. Müller-Buschbaum, Negative thermal expansion in one-dimension of a new double sulfate $AgHo(SO_4)_2$ with isolated SO_4 tetrahedra, J. Mater. Sci. Technol. 76 (2021) 111–121.
[13] W. Hisinger, J.B. Berzelius, Cerium, Ann. Chim. 50 (1804) 245–259.
[14] C. Tunsu, M. Petranikova, M. Gergorić, C. Ekberg, T. Retegan, Reclaiming rare earth elements from end-of-life products: A review of the perspectives for urban mining using hydrometallurgical uni toperations, Hydrometallurgy 156 (2015) 239–258.
[15] Z. Zhu, Y. Pranolo, C.Y. Cheng, Chu Yong Cheng, Separation of uranium and thorium from rare earths for rare earth production - A review, Miner. Eng. 77 (2015) 185–196.
[16] D. Beltrami, G.-P. Deblonde, S. Bélair, V. Weigel, Sarah Bélair, Valérie Weigel, Recovery of yttrium and lanthanides from sulfate solutions with high concentration of iron and low rare earth content, Hydrometallurgy 157 (2015) 356–362.

[17] L.A. Diaz, T.E. Lister, J.A. Parkman, G.G. Clark, Comprehensive process for the recovery of value and critical materials from electronic waste, J. Clean. Prod. 125 (2016) 236–244.

[18] S.P. Kelley, J.S. Nuss, R.D. Rogers, Using crystal structures of ionic compounds to explore complexation and extraction of rare earth elements in ionic liquids. Application of Ionic Liquids on Rare Earth Green Separation and Utilization, Springer, Heidelberg, (2015), 21–42.

[19] Z. Zhao, Z. Qiu, J.i. Yang, S. Lu, L. Cao, W. Zhang, Y. Xu, Recovery of rare earth elements from spent fluid catalytic cracking catalysts using leaching and solvent extraction techniques, Hydrometallurgy 167 (2017) 183–188.

[20] Josefina Perles, Carlos Fortes-Revilla, Enrique Gutiérrez-Puebla, Marta Iglesias, M. ÁngelesMonge, Caridad Ruiz-Valero, Natalia Snejko, Synthesis, structure, and catalytic properties of rare-earth ternary sulfates, Chem. Mater. 17 (10) (2005) 2701–2706.

[21] Z. Deng, F. Bai, Y. Xing, N.a. Xing, L. Xu, Reaction in situ found in the synthesis of a series of lanthanide sulfate complexes and investigation on their structure, spectra and catalytic activity, Open J. Inorg. Chem. 03 (04) (2013) 76–99.

[22] S.P. Sirotinkin, V.A. Efremov, A.N. Pokrovskii, L.M. Kovba, Crystal structure of lithium praseodymium sulfate LiPr(SO$_4$)$_2$, Kristallografiya 23 (1978) 406–408.

[23] S.P. Sirotinkin, V.A. Efremov, L.M. Kovba, A.N. Pokrovskii, Crystal structure of lithium-europium double sulfate, Kristallografiya 22 (1977) 966–970.

[24] S.P. Sirotinkin, A.N. Pokrovskii, L.M. Kovba, Crystal structures of certain double and simple rare earth sulfates, Kristallografiya 26 (1981) 385–389.

[25] S.M. Chizhov, A.N. Pokrovskii, L.M. Kovba, The crystal structure of NaLa(SO$_4$)$_2$, Kristallografiya 26 (1981) 834–836.

[26] S.P. Sirotinkine, S.M. Tchijov, A.N. Pokrovskii, L.M. Kovba, Structure cristalline de sulfates doubles de sodium et de terresrares, J. Less-Comm. Metal. 58 (1) (1978) 101–105.

[27] P.A. Degtyarev, L.M. Kovba, A.N. Pokrovskii, Crystal structure of the anhydrous double sulfate KPr(SO$_4$)$_2$, Kristallografiya 23 (1978) 840–843.

[28] P.A. Degtyarev, F.M. Korytnaya, L.M. Kovba, A.N. Pokrovskii, Crystal structure of the anhydrous double sulfate of potassium and neodymium KNd(SO$_4$)$_2$, Vestnik Moskovskogo Universiteta – Khimiya 18 (1977) 705–708.

[29] L.D. Iskhakova, Y.M. Gasanov, V.K. Trunov, Crystal structure of the monoclinic modification of KNd(SO$_4$)$_2$, Zh. Strukt. Khim. 29 (1988) 95–99.

[30] N. Bukovec, V. Kaucic, L. Golic, Cesium lanthanum bis (sulphate), Acta Cryst. B 36 (1980) 129–130.

[31] N. Bukovec, L. Golic, P. Bukovec, J. Siftar, Die Synthese und Kristallstruktur von Caesium-Praseodymsulfat, Monat. Chem. 109 (1978) 1305–1310.

[32] Caridad Ruiz-Valero, Concepción Cascales, Berta Gómez-Lor, Enrique Gutiérrez-Puebla, Marta Iglesias, M. Angeles Monge, Natalia Snejko, New catalytically active neodymium sulfate, J. Mater. Chem. 12 (2002) 3073-3077.

[33] Y.G. Denisenko, V.V. Atuchin, M.S. Molokeev, A.S. Aleksandrovsky, A.S. Krylov, A.S. Oreshonkov, S.S. Volkova, O.V. Andreev, Structure, thermal stability, and spectroscopic properties of triclinic double sulfate AgEu(SO$_4$)$_2$ with isolated SO$_4$ groups, Inorg. Chem. 57 (21) (2018) 13279–13288.

[34] AnhThy Bui, Alexei Grichine, Sophie Brasselet, Alain Duperray, Chantal Andraud, Olivier Maury, Unexpected Efficiency of a Luminescent Samarium (III) Complex for Combined Visible and Near-infrared Biphotonic Microscopy, Chem.–Eur. J. 21 (49) (2015) 17757–17761.

[35] R.D. Dominguez, G. Alarcón-Flores, M. Aguilar-Frutis, R.I. Sánchez-Alarcón, C. Falcony, H.J. Dorantes-Rosales, J.L. González-Velázquez, D.I. Rivas-López, Effect on the stabilization of the anatase phase and luminescent properties of samarium-doped TiO$_2$ nanocrystals prepared by microwave irradiation, J. Alloy Compd. 687 (2016) 121–129.

[36] H. Guan, Y.e. Sheng, Y. Song, K. Zheng, C. Xu, X. Xie, Y. Dai, H. Zou, White light-emitting, tunable color luminescence, energy transfer and paramagnetic properties of terbium and samarium doped BaGdF$_5$ multifunctional nanomaterials, RSC Adv. 6 (77) (2016) 73160–73169.

[37] H.A. Othman, H.S. Elkholy, I.Z. Hager, Spectroscopic investigation of samarium-doped lead oxyflouroborate glasses using photo and cathode luminescence, Int. J. Appl. Glass Sci. 8 (3) (2017) 313–321.

[38] M. Sobczyk, D. Szymański, M. Guzik, J. Legendziewicz, MałgorzataGuzik, Janina Legendziewicz, Optical behaviour of samarium doped potassium yttrium double phosphates, J. Lumin. 169 (2016) 794–798.

[39] S. Wang, JinXu, Juan Wang, Kai-yao Wang, Song Dang, Shuyan Song, Dan Liu, Cheng Wang, Luminescence of samarium (III) bis-dithiocarbamate frameworks: codoped lanthanide emitters that cover visible and near-infrared domains, J. Mater. Chem. C 5 (26) (2017) 6620–6628.

[40] S.Q. Mawlud, M.M. Ameen, M.R. Sahar, K.F. Ahmed, Plasmon-enhanced luminescence of samarium doped sodium tellurite glasses embedded with gold nanoparticles: Judd-Ofelt parameter, J. Lumin. 190 (2017) 468–475.

[41] N. Hamon, M. Galland, M. Le Fur, A. Roux, A. Duperray, A. Grichine, C. Andraud, B. Le Guennic, M. Beyler, O. Maury, R. Tripier, Combining a pyclen framework with conjugated antenna for the design of europium and samarium luminescent bioprobes, Chem. Commun. 54 (48) (2018) 6173–6176.

[42] J. Zhang, H. Riesen, Photostimulated and persistent luminescence of samarium ions in BaFCl, J. Lumin. 207 (2019) 188–194.

[43] V.V. Atuchin, C.C. Ziling, D.P. Shipilova, N.F. Beizel, Crystallographic, ferroelectric and optical properties of TiO$_2$-doped LiNbO$_3$ crystals, Ferroelectrics 100 (1) (1989) 261–269.

[44] V.V. Atuchin, C.C. Ziling, I. Savatinova, M.N. Armenise, V.M.N. Passaro, Waveguide formation mechanism generated by double doping in ferroelectric crystals, J. Appl. Phys. 78 (12) (1995) 6936–6939.

[45] H. Ji, Z. Huang, Z. Xia, M.S. Molokeev, V.V. Atuchin, S. Huang, Cation substitution dependent bimodal photoluminescence in whitlockite structural Ca$_{3-x}$Sr$_x$(PO$_4$)$_2$:Eu^{2+} ($0 \leq x \leq 2$) solid solution phosphors, Inorg. Chem. 53 (20) (2014) 11119–11124.

[46] G. Bulai, L. Diamandescu, I. Dumitru, S. Gurlui, M. Feder, O.F. Caltun, Effect of rare earth substitution in cobalt ferrite bulk materials, J. Magn. Magn. Mater. 390 (2015) 123–131.

[47] H. Ji, Z. Huang, Z. Xia, M.S. Molokeev, M. Chen, V.V. Atuchin, M. Fang, Yan'gai Liu, Xiaowen Wu, Phase transformation in Ca$_3$(PO$_4$)$_2$:Eu^{2+} via the controlled quenching and increased Eu^{2+} content: identification of new cyan-emitting α-Ca$_3$(PO$_4$)$_2$:Eu^{2+} phosphor, J. Am. Ceram. Soc. 98 (10) (2015) 3223–3230.

[48] Yi. Wei, Chun Che Lin, Zewei Quan, Maxim S. Molokeev, Victor V. Atuchin, Ting-Shan Chan, Yujun Liang, Jun Lin, Guogang Li, Structural evolution induced preferential occupancy of designated cation sites by Eu2+ in M5(Si3O9)2 (M = Sr, Ba, Y, Mn) phosphors, RSC Adv. 6 (2016) 57261–57265.

[49] X. Wang, X. Shi, M.S. Molokeev, Z. Wang, Q.i. Zhu, X. Li, X. Sun, J.-G. Li, NaLaW$_2$O$_7$(OH)$_2$(H$_2$O): Crystal structure and RE^{3+} luminescence in the pristine and annealed double tungstates (RE = Eu, Tb, Sm, and Dy), Inorg. Chem. 57 (2018) 13606–13617.

[50] Z. Zhou, N. Zhang, J. Chen, X. Zhou, M.S. Molokeev, C. Guo, The Vis-NIR multicolor emitting phosphor Ba$_4$Gd$_3$Na$_3$(PO$_4$)$_6$F$_2$: Eu^{2+}, Pr^{3+} for LED towards plant growth, J. Indust. Eng. Chem. 65 (2018) 411–417.

[51] Jinmeng Xiang, Jiming Zheng, Ziwei Zhou, HaoSuo, Xiaoqi Zhao, Xianju Zhou, Niumiao Zhang, Maxim S. Molokeev, Chongfeng Guo, Enhancement of red emission and site analysis in Eu2+ doped new-type structure Ba3CaK(PO4)3 for plant growth white LEDs, Chem. Eng. J. 356 (2019) 236–244.

[52] J. Qiao, M. Amachraa, M. Molokeev, Y.-C. Chuang, S.P. Ong, Q. Zhang, Z. Xia, Shyue Ping Ong, Qinyuan Zhang, Zhiguo Xia, Engineering of K$_3$YSi$_2$O$_7$ to tune photoluminescence with selected activators and site occupancy, Chem. Mater. 31 (18) (2019) 7770–7778.

[53] H. Ji, Z. Huang, Z. Xia, M.S. Molokeev, X. Jiang, Z. Lin, V.V. Atuchin, Comparative investigations of the crystal structure and photoluminescence property of eulytite-type Ba$_3$Eu(PO$_4$)$_3$ and Sr$_3$Eu(PO$_4$)$_3$, Dalton Trans. 44 (16) (2015) 7679–7686.

[54] N.N. Golovnev, M.S. Molokeev, S.N. Vereshchagin, V.V. Atuchin, Synthesis and thermal transformation of a neodymium(III) complex [Nd(HTBA)$_2$(C$_2$H$_3$O$_2$)(H$_2$O)$_2$]·2H$_2$O to non-centrosymmetric oxosulfate Nd$_2$O$_2$SO$_4$, J. Coord. Chem. 68 (11) (2015) 1865–1877.

[55] I.A. Razumkova, A.N. Boiko, O.V. Andreev, S.A. Basova, Synthesis of [(H$_3$O) Tm$_3$F$_{10}$]·nH$_2$O, ErF$_3$, and TmF$_3$ powders and their physicochemical properties, Russ. J. Inorg. Chem. 62 (4) (2017) 418–422.

[56] Y.G. Denisenko, N.A. Khritokhin, O.V. Andreev, S.A. Basova, E.I. Sal'nikova, A.A. Polkovnikov, Thermal decomposition of europium sulfates Eu$_2$(SO$_4$)$_3$·8H$_2$O and EuSO$_4$, J. Solid State Chem. 255 (2017) 219–224.

[57] X. Wang, M.S. Molokeev, Q.i. Zhu, J.-G. Li, Controlled hydrothermal crystallization of anhydrous Ln$_2$(OH)$_4$SO$_4$ (Ln = Eu-Lu, Y) as a new family of layered rare earth matelhydrooxides, Chem. Eur. J. 23 (2017) 16034–16043.

[58] Y.G. Denisenko, A.S. Aleksandrovsky, V.V. Atuchin, A.S. Krylov, M.S. Molokeev, A.S. Oreshonkov, N.P. Shestakov, O.V. Andreev, Exploration of structural, thermal and spectroscopic properties of self-activated sulfate Eu$_2$(SO$_4$)$_3$ with isolated SO$_4$ groups, J. Indust. Eng. Chem. 68 (2018) 109–116.

[59] O.V. Andreev, I.A. Razumkova, A.N. Boiko, Synthesis and thermal stability of rare earth compounds REF$_3$, REF$_3$·nH$_2$O and (H$_3$O)RE$_3$F$_{10}$·nH$_2$O (RE = Tb-Lu, Y), obtained from sulphide precursors, J. Fluorine Chem. 207 (2018) 77–83.

[60] V.V. Atuchin, O.D. Chimitova, S.V. Adichtchev, J.G. Bazarov, T.A. Gavrilova, M.S. Molokeev, N.V. Surovtsev, Z.G. Bazarova, Synthesis, structural and vibrational properties of microcrystalline β-RbSm(MoO$_4$)$_2$, Mater. Lett. 106 (2013) 26–29.

[61] Bruker AXS TOPAS V4: General profile and structure analysis software for powder diffraction data. – User's Manual. Bruker AXS, Karlsruhe, Germany. 2008.

[62] R.L. Blaine, H.E. Kissinger, Homer Kissinger and the Kissinger equation, Thermochim. Acta 450 (2012) 1–6, https://doi.org/10.1016/j.tca.2012.04.008.

[63] N. Bukovec, P. Bukovec, J. Šiftar, Kinetics of the thermal decomposition of Pr$_2$(SO$_4$)$_3$ to Pr$_2$O$_2$SO$_4$, Thermochim. Acta 35 (1) (1980) 85–91, https://doi.org/10.1016/0040-6031(80)85025-8.

[64] J. Llópiz, M.M. Romero, A. Jerez, Y. Laureiro, Generalization of the Kissinger equation for several kinetic models, Thermochim. Acta 256 (2) (1995) 205–211, https://doi.org/10.1016/0040-6031(94)02109-2.

[65] A.S. Lyadov, V.V. Kurilkin, Reduction specifics of rare-earth orthovanadates (REE = La, Nd, Sm, Dy, Ho, Er, Tm, Yb, and Lu), Russ. J. Inorg. Chem. 61 (2016) 86–92, https://doi.org/10.1134/S003602361601015.

[66] O. Lindgren, L. Oinonen, P. Salomaa, H. Svanholt, P. Hagenmuller, A.F. Andresen, The crystal structure of sodium cerium(III) sulfate hydrate, NaCe (SO$_4$)$_2$(H$_2$O), Acta Chem. Scand. A 31a (1977) 591–594.

[67] A.C. Blackburn, R.E. Gerkin, Sodium lanthanum(III) sulfate monohydrate, NaLa (SO$_4$)$_2$×·H$_2$O, Acta Cryst. C 50 (6) (1994) 835–838.

[68] A.C. Blackburn, R.E. Gerkin, Redetermination of sodium cerium(III) sulfate monohydrate, NaCe(SO$_4$)$_2$·H$_2$O, Acta Cryst. C 51 (11) (1995) 2215–2218.

[69] C.-D. Wu, Z.-Y. Liu, Hydrothermal synthesis of a luminescent Europium(III) sulfate with three-dimensional chiral framework structure, J. Solid State Chem. 179 (11) (2006) 3500–3504.

[70] B. Zhai, Z. Li, C. Zhang, F. Zhang, X. Zhang, F. Zhang, G. Cao, S. Li, X. Yang, Three rare Ln–Na heterometallic 3D polymers based on sulfate anion: Syntheses, structures, and luminescence properties, Inorg. Chem. Commun. 63 (2016) 16–19.

[71] A.K. Paul, R. Kanagaraj, Synthesis, characterization, and crystal structure analysis of new mixed metal sulfate NaPr(SO$_4$)$_2$(H$_2$O), J. Struct. Chem. 60 (3) (2019) 477–484.

[72] P.N. Iyer, P.R. Natarajan, Double sulfates of plutonium(III) and lantanides with sodium, J. Less-Comm. Metals 148 (1–2) (1989) 161–166.

[73] R.D. Shannon, Revised effective ionic radii and systematic studies of interatomic distances in halides and chalcogenides, Acta Cryst. A 32 (5) (1976) 751–767.

[74] E. Kroumova, M.I. Aroyo, J.M. Perez-Mato, A. Kirov, C. Capillas, S. Ivantchev, H. Wondratschek, Bilbao Crystallographic Server : Useful databases and tools for phase-transition studies, Phase Transit. 76 (1-2) (2003) 155–170.

[75] K. Nakamoto, Infrared and Raman Spectra of Inorganic and Coordination Compounds, 6th edn., Wiley, New York, 2009.

[76] V.V. Atuchin, A.S. Aleksandrovsky, M.S. Molokeev, A.S. Krylov, A.S. Oreshonkov, D.i. Zhou, Di Zhou, Structural and spectroscopic properties of self-activated monoclinic molybdate $BaSm_2(MoO_4)_4$, J. Alloys Compd. 729 (2017) 843–849.

[77] Yu.G. Denisenko, E.I. Sal'nikova, S.A. Basova, M.S. Molokeev, A.S. Krylov, A.S. Aleksandrovsky, A.S. Oreshonkov, V.V. Atuchin, S.S. Volkova, N.A. Khritokhin, O.V. Andreev, Synthesis of samarium oxysulfate $Sm2O2SO4$ in the high-temperature oxidation reaction and its structural, thermal and luminescence properties, Molecules 25 (2020) 1330.

[78] R.A. Lidin, L.L. Andreeva, V.A. Molochko, Inorganic Constants: a Handbook, Drofa, Moscow, 2006.

[79] O.V. Andreev, Yu.G. Denisenko, S.A. Osseni, V.G. Bamburov, E.I. Sal'nikova, N.A. Khritokhin, P.O. Andreev, A.A. Polkovnikov, Sulfates and oxysulfides of rare-earth elements: Monograph, UTMN Publ. Tyumen. (2017).

[80] S. Cheng, Y. Wu, D. Mei, S. Wen, T. Doert, Synthesis, crystal structures, spectroscopic characterization, and thermal analyses of the new bismuth sulfates $NaBi(SO_4)_2 \cdot H_2O$ and $ABi(SO_4)_2$ (A= K, Rb, Cs), Z. Anorg. Allgem. Chem. 646 (20) (2020) 1688–1695.

[81] Yuriy G. Denisenko, Alexander E. Sedykh, Maxim S. Molokeev, Aleksandr S. Oreshonkov, Aleksandr S. Aleksandrovsky, Alexander S. Krylov, Nikolay A. Khritokhin, Elena I. Sal'nikova, Oleg V. Andreev, Klaus Müller-Buschbaum, Crystal and electronic structure, thermochemical and photophysical properties of europium-silver sulfate monohydrate AgEu(SO4)2·H2O, J. Solid State Chem. 294 (2021) 121898.